Available online at www.sciencedirect.com

ScienceDirect

Advances in Space Research 75 (2025) 3661–3670

ADVANCES IN SPACE RESEARCH (a COSPAR publication)

www.elsevier.com/locate/asr

Tunneling of acoustic-gravity waves through critical levels to the upper atmosphere

N.M. Gavrilov [a,*], S.P. Kshevetskii [a,b,d], A.V. Koval [a], Yu.A. Kurdyaeva [c]

[a] Saint-Petersburg State University, Saint Petersburg, Russia
[b] I. Kant Baltic Federal University, Kaliningrad, Russia
[c] West Department of Pushkov Institute of Terrestrial Magnetism, Ionosphere and Radio Wave Propagation, Russian Academy of Sciences, Kaliningrad, Russia
[d] A. M. Obukhov Institute of Atmospheric Physics, Russian Academy of Sciences, Moscow, Russia

Received 18 June 2024; received in revised form 29 November 2024; accepted 3 December 2024
Available online 6 December 2024

Abstract

Using a high-resolution nonlinear numerical model, simulations are performed to study the propagation of acoustic-gravity waves (AGWs) from the troposphere into the upper atmosphere. These simulations take into account background wind profiles containing critical levels, where the horizontal wind velocity becomes equal to the horizontal AGW phase speed. According to conventional linear theories of atmospheric waves, the vertical wavelength approaches zero near critical levels, resulting in strong dissipation of AGWs propagating from the troposphere and preventing them from reaching the upper atmosphere. Our numerical simulations are carried out using wave sources in the form of plain wave perturbations of vertical velocity, propagating along the Earth's surface. Jet streams in the atmosphere are approximated by Gaussian profiles of the mean zonal wind with maxima located at altitudes of 110 km and 50 km. Calculations reveal that AGW amplitudes are significantly reduced above the high-altitude critical levels. For the critical levels at altitudes 30–70 km, part of wave energy can penetrate through them and propagate further into the upper atmosphere. In the nonlinear model, increased generation of secondary wave modes occur near the critical level. Therefore, modes with vertical wavelengths longer than that of the primary AGW dominate at altitudes exceeding 130 km, where amplitudes of these secondary waves may surpass the amplitudes of the primary AGW in the absence of middle atmosphere critical levels.

Keywords: Acoustic-gravity waves; Critical level; Secondary waves; Numerical simulation; Upper atmosphere

1. Introduction

An important role in the dynamics of the middle and upper atmosphere belongs to acoustic-gravity waves (AGWs). The waves generated in the lower atmosphere propagate upwards into the mesosphere and thermosphere, transferring momentum and energy to higher layers of the atmosphere (e.g., Vadas and Liu, 2013; Franco-Diaz et al., 2024). Due to dissipation and momentum transfer to the mean flow, AGWs can change the zonal wind in the mesosphere and lower thermosphere and affect the general circulation of the middle and upper atmosphere (Holton, 1983). Numerous studies (e.g., Miyoshi et al., 2014; Becker and Vadas, 2020) have shown that wave accelerations of the mean flow caused by dissipating AGWs coming from the

* Corresponding author.
E-mail addresses: n.gavrilov@spbu.ru (N.M. Gavrilov), renger@mail.ru (S.P. Kshevetskii), a.v.koval@spbu.ru (A.V. Koval), yakurdyaeva@gmail.com (Y.A. Kurdyaeva).

https://doi.org/10.1016/j.asr.2024.12.005

troposphere play an important role in maintaining the momentum balance in the thermosphere (Becker and Vadas, 2020). Thus, understanding the dynamics of the atmosphere as a whole and interactions between its layers requires adequate knowledge of AGWs.

To take into account AGW effects in global circulation models, subgrid mesoscale waves and their interaction with the mean flow should be parameterized, and these parameterizations should be compared with observations and results of high-resolution modeling (e.g., Alexander et al., 2010; Geller et al., 2013; Becker and Goncharenko, 2022b; Vadas et al, 2023a, 2024). Nowadays, numerical models of global circulation having high resolution (e.g., Miyoshi and Fujiwara, 2008; Becker et al., 2015) can simulate medium to large-scale AGWs. For example, the Hi Altitude Mechanistic general Circulation Modes (HIAMCM) can explicitly simulate AGWs with horizontal wavelengths of 200 to thousands km (Becker & Vadas, 2020, Vadas et al, 2023a, 2024). Results of High-resolution global circulation models agree well with the data on gravity waves in the thermosphere and ionosphere (Vadas et al, 2023b, Vadas et al, 2023a, 2024).

Numerical simulation of nonlinear small-scale waves and turbulence in the atmosphere has been rapidly developing in recent years. Fritts et al. (2009, Fritts et al., 2014) have simulated the breaking of atmospheric internal waves and Kelvin—Helmholtz instabilities. Their models are three-dimensional and describe the propagation and breaking of AGWs in atmospheric regions with limited horizontal and vertical dimensions. Numerical two-dimensional models of AGWs in the atmosphere were developed by Liu et al. (2008) and Yu et al. (2009). A two-dimensional ICON model was exploited by Gassmann and Herzog (2015).

AGWs break in the atmosphere at altitudes up to 200 km (Lund and Fritts, 2012, Vadas and Liu, 2013). AGW breaking is strongly nonlinear and produce a cascade and transfer of energy to smaller-scale spectral components. Smaller-scale secondary wave modes are shorter than primary breaking AGWs (Heale et al., 2022; Gavrilov et al., 2022; Gavrilov and Kshevetskii, 2023). These secondary AGWs can create substantial wave fluxes of momentum, and can increase the wave energy transfer into turbulence. The deposition of momentum and energy that occurs during and after wave breaking and the cascade to turbulence can generate a 2nd type of secondary AGWs (Vadas et al. 2003, 2018). This latter wave type tends to have larger horizontal wavelengths and phase speeds compared to the primary AGW. They can transfer energy and momentum more effectively and propagate to higher altitudes in the upper atmosphere (Vadas and Liu, 2013; Becker and Goncharenko, 2022b; Vadas et al, 2024). Secondary AGWs of the 2nd type have been observed with a lidar in the stratosphere and mesosphere (Vadas et al., 2023a), as well as in the MLT region and in the thermosphere (Vadas et al., 2024), including in the thermosphere and ionosphere after the Tonga eruption (Vadas et al. 2023b, 2023c).

The primary AGWs that propagate from the troposphere can create localized regions of increased and decreased momentum and energy fluxes in the middle and upper atmosphere (Fritts et al., 2006; Smith et al., 2016; Vadas and Becker, 2019). Inhomogeneities of the respective wave drag may generate downward and upward propagating secondary modes having horizontal wavelengths, which depend on scales of the irregularities (Vadas et al., 2003). Primary AGW breaking accompanied by increased nonlinearity can also generate secondary waves. Such secondary AGWs arise as higher harmonics and usually have lengths and periods shorter than primary wave modes (Bacmeister and Schoeberl, 1989; Franke and Robinson, 1999). Since most secondary waves have larger phase velocities and longer vertical wavelengths, they may reach higher altitudes. Large-amplitude secondary waves can, in turn, break and cause additional accelerations at high altitudes (Vadas and Becker, 2019; Becker and Vadas, 2020; Vadas et al, 2024).

An important source of AGWs observed in the middle atmosphere is the tropospheric deep convection (e.g., Franco-Diaz et al., 2024). Simulation has shown that the primary AGWs excited by deep convection can reach the thermosphere, where they break and dissipate (Vadas and Crowley, 2010; Vadas and Liu, 2013). This process produces spatially and temporally-localized horizontal wave accelerations, which generate longer secondary AGWs (Vadas and Liu, 2013). Such secondary AGWs can then propagate to much higher altitudes, leading to considerable variability in the neutral wind (Vadas and Crowley, 2017). Furthermore, these secondary AGWs increase the variability of the ionosphere by generating medium- and large-scale traveling ionospheric disturbances (Vadas et al., 2021). Perturbations formed in the winter polar stratosphere were observed in the mesosphere and lower thermosphere (Chen et al., 2016; Zhao et al., 2017), and were found to agree well with the modeled wintertime secondary AGWs (Becker and Vadas, 2018). Analysis of concentric wave fronts in the middle and upper atmosphere produced by a typhoon (Li et al, 2022) reveals an important role of secondary waves in the formation of AGW fields in the thermosphere. Generation of secondary AGWs is an important process that can strongly modify the wave energy and momentum transfer and transformation mechanisms. Deeper research of secondary waves needs further development of numerical high-resolution models and methods for distinguishing the spectra of primary and secondary waves.

Gavrilov and Kshevetskii (2014) have developed a high-resolution three-dimensional numerical model describing the propagation of nonlinear AGWs through the atmosphere from the Earth's surface to the thermosphere. The numerical scheme adequately takes into account the fundamental laws of conservation of mass, momentum, and

energy, as well as the law of non-decreasing entropy. This model can provide physically correct generalized solutions of hydrodynamic equations and ensure the stability of the numerical scheme in the field of breaking nonlinear waves and transition to turbulence, where many computational algorithms become invalid. With the wide range of heights under study, this stable algorithm makes the numerical model suitable for simulating AGWs and their instability at heights from the Earth's surface to the thermosphere. Numerical simulation provides further insight into the mechanisms of dynamic interaction between different atmospheric layers.

This article describes simulating primary plane waves in the high-resolution model AtmoSym (2017), which propagate to the upper atmosphere through the mean wind profiles, containing critical levels, where the mean wind velocity is equal to the horizontal phase speed of the primary wave. We consider a high-altitude jet stream with maximum velocity at 110 km altitude. Such strong jet streams were observed in the upper atmosphere (e.g., Larsen, 2000; Larsen et al., 2005). For comparison, we consider a jet stream located in the middle atmosphere, which can represent stratosphere-mesosphere circulation flows and, in particular, the polar vortex jets, which are wintertime phenomena in the norther and southern hemispheres. Differences are considered of AGW propagation to the thermosphere through such jet streams located at different atmospheric altitudes.

2. Numerical model

We have used a high-resolution three-dimensional numerical model "AtmoSym" developed by Gavrilov and Kshevetskii (2014), which is available online for free (AtmoSym, 2017). The model is based on the plane geometry and complete hydrodynamic three-dimensional equations (Gavrilov et al., 2022). The AtmoSym model takes into account dissipative and nonlinear processes affecting AGW propagation, and can describe such complex processes as instability of AGWs, their breaking and turbulence generation. The model was verified and gives ratios of different hydrodynamic parameters close to theoretical AGW polarization relations, when nonlinearity and dissipation are weak (Gavrilov et al., 2015).

Background temperature profiles $T_0(z)$ for the simulation have been taken from the semi-empirical atmospheric model NRLMSISE-00 (Picone et al., 2002). Background dynamic coefficients of molecular viscosity and thermal conductivity are estimated using Sutherland's formula (Kikoin, 1976). The lower boundary of the model is located at the Earth's surface. The AtmoSym model also includes background turbulent viscosity and thermal conductivity that reach maxima of ~10 m^2/s in the boundary layer and the lower thermosphere and a minimum of 0.1 m^2/s in the stratosphere (Gavrilov and Kshevetskii, 2014).

Zero values of vertical gradients of temperature and horizontal velocity, as well as zero vertical velocity are set at the upper boundary (Gavrilov et al., 2022). Under such upper boundary conditions, the AGWs coming from the underlying layers of the atmosphere may be reflected. The upper boundary in the present study is set at the altitude of 600 km, where molecular viscosity and thermal conductivity are very high, and the reflected waves are subjects to strong attenuation. Numerical tests indicate that the influence of upper boundary conditions is negligible at distances from the upper boundary that are twice the atmospheric scale height. Thus, at analyzed altitudes up to 200 km, the influence of upper boundary conditions is insignificant. Gavrilov et al. (2015, 2022) simulated nonlinear AGW propagation from lower boundary forcing having forms of plane waves. In the present study, we assume horizontally periodical distributions of vertical velocity at the Earth's surface of the form of

$$(w)_{z=0} = W_0 cos[k_x(x - c_x t)] cos[k_y(y - c_y t)], \quad (1)$$

where k_x, k_y and c_x, c_y are wavenumbers and phase velocities along horizontal axes x and y, respectively; W_0 is the wave forcing amplitude. Eq. (1) represents horizontally moving periodical structures of vertical velocity at the bottom boundary. Forcing of Eq. (1) may simulate spectral Fourier-components of convective and turbulent AGW sources transported by the mean winds in the atmosphere (Townsend 1965, 1966). Considerations of the plane wave source Eq. (1) allows comparisons of numerical model results with conventional AGW theories (e.g., Gossard and Hooke, 1975), which also consider properties of individual plane Fourier-components. In the present paper we made calculations for different c_x between 10 and 100 ms^{-1} at $k_y = 0$. In this case, Eq. (1) describes waves propagating along the horizontal axis x with stationary amplitude along the axis y.

Our numerical simulations were made using zero initial conditions for wave fields at the moment $t = 0$ of activating the wave source Eq. (1) at the lower boundary. To reduce the pace of the activation of the wave source, we multiply W_0 in Eq. (1) by a Gaussian factor

$$q(t) = \begin{cases} \exp\left[-(t - t_a)^2/s_a^2\right] & at\ t \le t_a \\ 1 & at\ t > t_a \end{cases} \quad (2)$$

changing from zero at $t = 0$ to 1 at the moment $t = t_a$, which we consider as the time of the wave source activation (see Gavrilov et al., 2022). At $t > t_a$, the source amplitude W_0 does not change and allows obtaining quasi-stationary AGW regime at large t. At low W_0 in Eq. (1), in the lower and middle atmosphere at $t >> t_a$ the numerical solution tends to plane steady-state waves, which match traditional linear AGW theory (e.g., Gossard and Hooke, 1975). Gavrilov et al. (2015) obtained fair agreement between the simulated ratios of amplitudes of different wave parameters and the polarization relations of the linear AGW theory (Gossard and Hooke, 1975) at altitudes to 100 km at $t >> t_a$.

3. Results of simulations

Medvedev and Gavrilov (1995) analyzed AGW generation by nonlinear interactions caused by meteorological and turbulent motions in the atmosphere. They found that such interactions could produce components of wave spectra having broad variety of amplitudes, wavelengths and other parameters. IGW simulations with the AtmoSym high-resolution nonlinear model are made in the atmospheric domain with horizontal dimensions of 800 km with lower boundary at the Earth's surface and upper boundary at altitude of 600 km. Here we consider two primary IGW modes with the horizontal wavelength $\lambda_x = 2\pi/k_x = 200$ km and phase speeds of $c_x = 30$ m/s or $c_x = 60$ m/s in the wave source of Eq. (1) with $W_0 = 0.1$ mm/s at the lower boundary and smooth wave source triggering at $s_a = 10^3$ s in Eq. (2). This corresponds to the periods of the primary modes $\tau = \lambda_x/c_x = 6.67{\cdot}10^3$ s and $\tau = 3.33{\cdot}10^3$ s for the above c_x values, respectively. The spacing of the horizontal grid of the model is $\Delta x = \lambda_x/32 = 6.4$ km. The spacing of the vertical grid is determined automatically depending on the atmospheric scale height and vary from about 12 m near the ground to several km at altitudes above 200 rm. The time step of the simulations is determined automatically to provide stability of numerical algorithm and it is about a few seconds.

Gavrilov and Kshevetskii (2014) showed that triggering the plane wave forcing at the lower boundary produces pulses of acoustic waves propagating upwards. Calculations show that in the horizontally periodical excitation of Eq. (1), these acoustic disturbances have the form of quasi-vertically propagating perturbations similar to those in Fig. 1a–c of the paper by Gavrilov and Kshevetskii (2014). These perturbations in a few minutes can arrive at altitudes of 100 km and above, where acoustic waves can have substantial amplitudes.

Fig. 1 shows examples of simulated wave structures in the windless atmosphere with a realistic vertical temperature profile for sufficiently late instances t after activating the wave forcing Eq. (1) with different c_x. One can see the surfaces of constant phase inclined to the horizon below 100 km altitudes, which are characteristic for the branch of low-frequency atmospheric AGWs called as internal gravity waves (IGWs). A theory of plane linear stationary IGWs (e.g., Gossard and Hooke 1975) gives the angle of this inclination to be $arcsin(\tau_N/\tau_i)$, where τ_N and τ_i are the Brunt-Vaisala and IGW intrinsic periods, respectively. This corresponds to the theoretical vertical wavelength $\lambda_z \approx c_{xi}\tau_N$, where c_{xi} is the intrinsic horizontal phase speed. This gives $\lambda_z \sim$ 9–12 km for $c_{xi} = 30$ ms^{-1} and $\lambda_z \sim$ 18–24 km for $c_{xi} = 60$ ms^{-1} at typical $\tau_N \sim (3–4){\cdot}10^2$ s at altitudes 50–100 km in January.

One may calculate effective simulated λ_z as the mean vertical separation of quasi-linear inclined wave fronts in Fig. 1. This gives $\lambda_z \approx 10$ km for $c_x = 30$ ms^{-1} at altitudes 50 – 100 km in the right panel of Fig. 1. Similar estimations for the left panel of Fig. 1 at $c_x = 60$ ms^{-1} give, respectively, $\lambda_z \approx 20$ km. This shows that in both cases λ_z tends

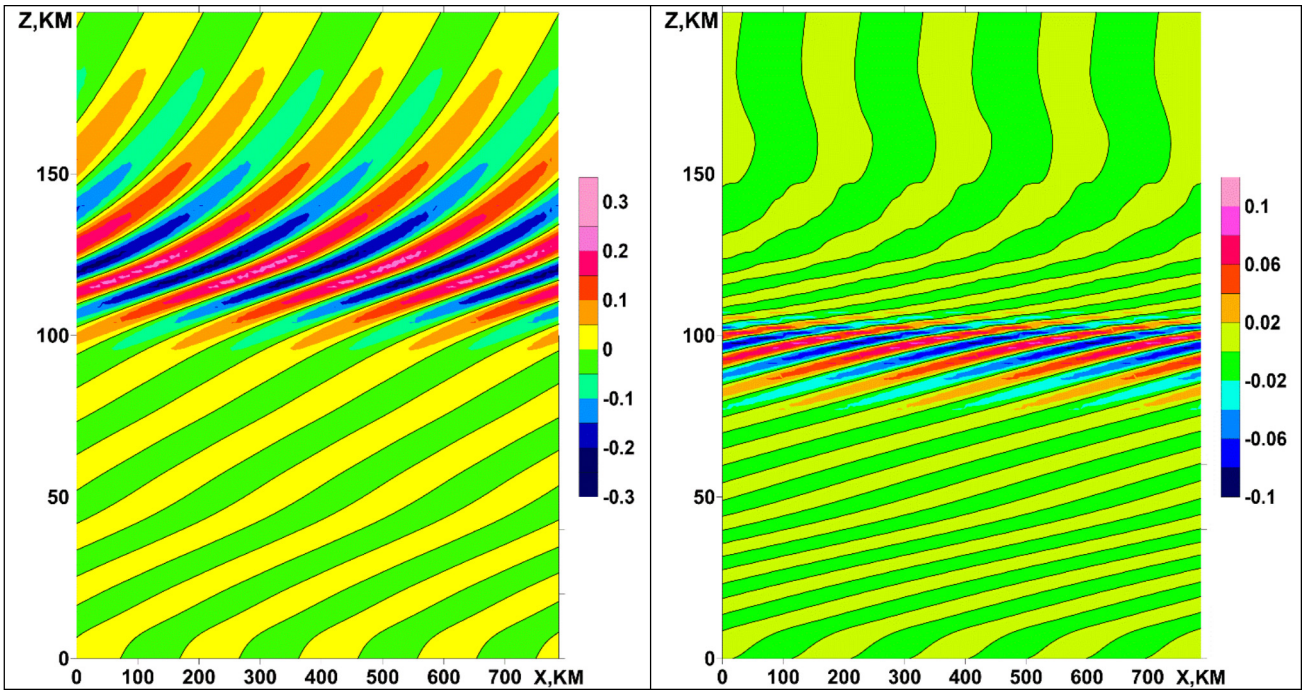

Fig. 1. XOZ cross-sections of wave fields of vertical velocity in m/s for AGWs with $c_x = 60$ m/s at the model time $t = 150$ h (left) and with $c_x = 30$ m/s at $t = 75$ h (right) in the windless atmosphere with realistic vertical temperature profile.

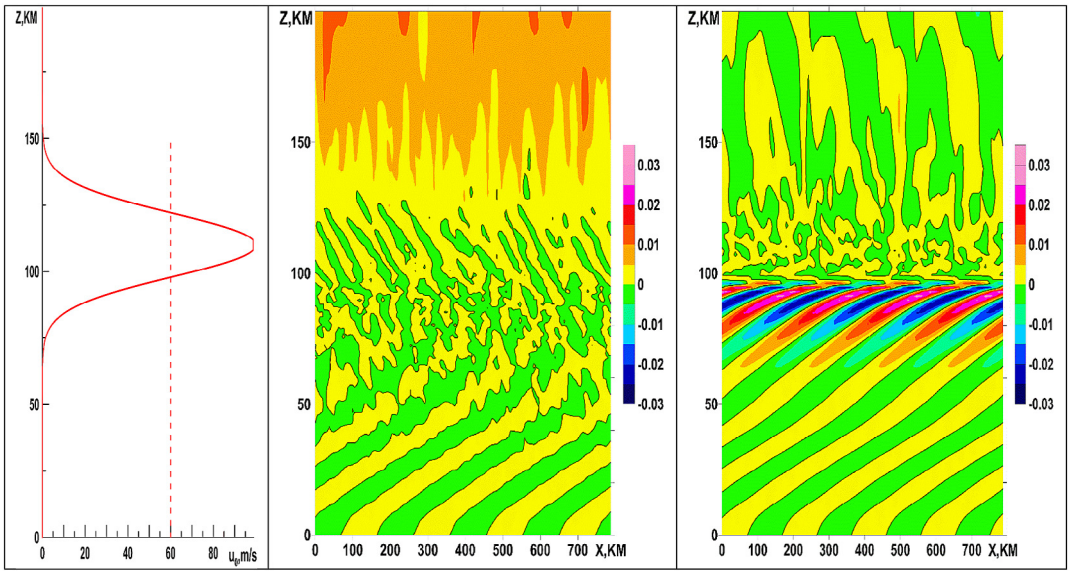

Fig. 2. The mean wind profile (left) and XOZ cross-sections of wave fields of vertical velocity in m/s for AGW with $c_x = 60$ m/s at the model time $t = 7$h (middle) and $t = 150$ h (right). Dashed line corresponds to the wave phase velocity and marks the critical levels.

to the theoretically predicted ranges of values (see above) after a transition interval, which can last more than ten periods τ of the used wave forcing (see above).

Fig. 2 shows simulated vertical velocity field for AGW source of Eq. (1) with $c_x = 60$ m/s at two different time instances for the high-altitude jet stream with the profile of horizontal mean velocity shown in the left panel of Fig. 2. The mean wind profile was prescribed at the initial moment and it can slightly evolve during the simulation. There are two critical levels, where the mean wind profile crosses the dashed line corresponding to the AGW horizontal phase speed in the left panel of Fig. 2. One can see that shortly after turning on the boundary wave source Eq. (1), in the middle panel of Fig. 2, initial transient AGW pulses can go through the critical level. However, later, in the right panel of Fig. 2, IGWs go up to the critical level, their vertical wavelengths decrease and they are subjects to strong dissipation due to high molecular viscosity and heat conductivity. Therefore, IGW amplitudes in the right panel of Fig. 2 above altitude of 120 km are several orders of magnitude smaller than those in the left panel of Fig. 1 for the same model time and $c_x = 60$ m/s, but without the critical levels.

Fig. 3 is analogous to Fig. 2, but for the jet stream located in the middle atmosphere with maximum at altitude of 50 km and for AGW with $c_x = 30$ m/s. Consideration of the right panel of Fig. 3 shows that the viscosity and heat conduction in the middle atmosphere is not strong enough for total dissipation of wave modes with medium and long horizontal and vertical wavelengths propagating from below near the critical level. Therefore, part of wave energy may tunnel upwards and substantial wave perturbations occur above the jet stream in the right panel of Fig. 3. Substantial contribution may give so called secondary wave modes, which can be generated in the atmosphere due to nonlinear interactions and dissipating primary IGWs (Heale et al., 2022; Vadas et al., 2018).

Between altitudes 40 and 60 km, the main wave fronts are inclined to the horizon in the direction opposite to that outside these altitudes in the right panel of Fig. 3. This layer is located between the lower and upper critical levels, where horizontal velocity of the mean wind exceeds the wave horizontal phase speed of the primary wave, the respective intrinsic frequency becomes negative. Therefore, maintaining positive wave energy flux and positive vertical group speed $c_{gz} \sim -\omega/m$ requires respective change in the sign of the vertical wavenumber m from negative to positive, which correspond to upward phase propagation between altitudes 40 and 60 km in Fig. 3 for $c_x = 30$ m/s and downward phase propagation outside this layer. Vadas et al. (2023a) found evidences about generating upward and downward propagating secondary IGWs within the polar vortex jet in the stratosphere.

The right panel of Fig. 1 shows relatively small amplitudes of IGW with $c_x = 30$ m/s at altitudes above 120 km with four maxima and four minima in the horizontal direction corresponding to the primary wave structure. The right panel of Fig. 3 shows two–three times more maxima and minima at altitudes above 100 km. This shows the generation of secondary waves, which may have horizontal lengths 2–3 times shorter than that of the primary IGW and may dominate in the upper atmosphere above the jet stream. Simulations of AGW spectrum developments in the AtmoSym high-resolution nonlinear model showed that modes with the horizontal length 1/2 and 1/3 of that of primary IGW indeed have largest amplitudes in the spectrum of secondary wave modes in the atmosphere (Gavrilov and Kshevetskii, 2023; Efimov et al., 2023).

The spectrum of secondary waves may contain components with longer vertical wavelengths, which are less dissi-

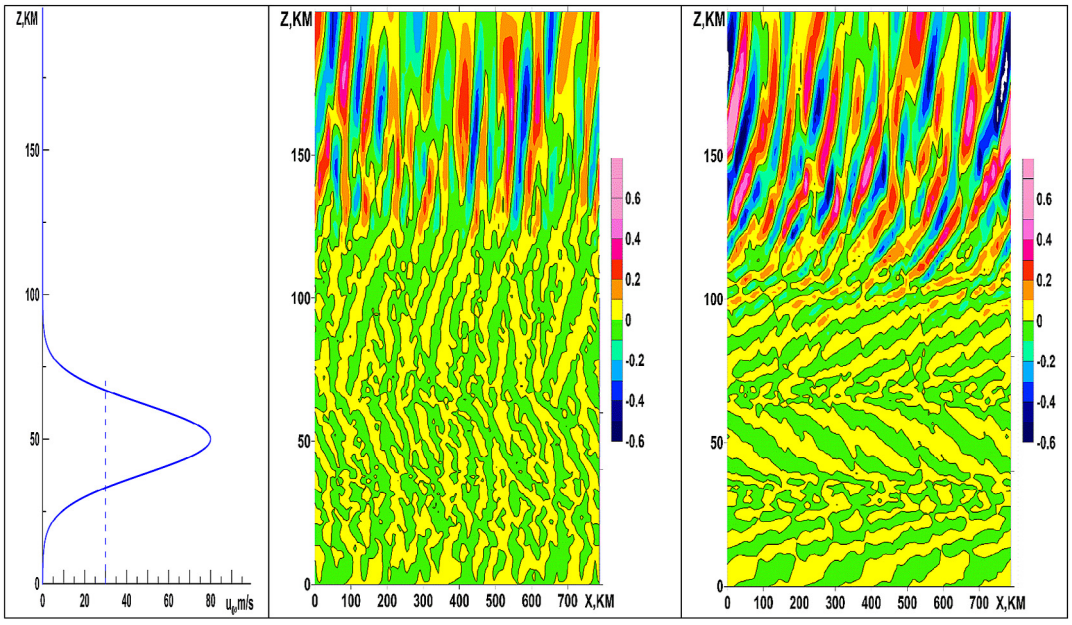

Fig. 3. Same as Fig. 2, but for AGW with $c_x = 30$ m/s at the model time $t = 5$h (middle) and $t = 75$ h (right).

pative due to molecular and turbulent viscosity and heat conduction (Vadas, 2007), so that their amplitudes above the critical layer in the right panel of Fig. 3 are much larger at high altitudes, than the amplitudes in the right panel of Fig. 1 for the primary IGW. This may confirm the results by Zhao et al. (2017), who observed that IGWs registered at altitudes near 30 km have frequently shorter vertical wavelengths than waves at altitudes 60–65 km and supposed that shorter waves dominated in the stratosphere may generate secondary waves, which can propagate upwards and be persistently observed at higher altitudes.

4. Discussion

The problem of critical levels appeared in the wave theory due to singular points, where coefficients of linearized wave equations (e.g., Gossard and Hooke, 1975) tend to infinity. For a particular Fourier-component with observable frequency σ and horizontal wave number k, such singularity appears, when the intrinsic frequency $\omega = \sigma - kv_0 \to 0$ that is equivalent to $c_h \to v_0$ (where $c_h = \sigma/k$ is the horizontal phase speed, v_0 is the component of mean wind along the horizontal wave vector). The left panels of Figs. 2 and 3 show the existence of two critical levels in the gaussian mean wind profiles: in the lower and upper parts of the stream, where $v_0 = c_h$.

Vertical group velocity $c_{gz} \sim -\omega/m \to 0$ near the critical level. This means that the wave energy should go quasi-horizontally along the critical level and the IGW should be subject to strong dissipation (as far as $|m| \to \infty$) in the vicinity of the critical level. Such behavior one can see in the right panel of Fig. 2 for high-altitude jet stream. The IGW trajectories become quasi-horizontal near the critical level just below 100 km altitude. Strong molecular and turbulent viscosity and heat conduction provide strong dissipation of wave energy near the critical level. Therefore, wave amplitudes in the right Fig. 2 at altitudes above 120 km are much smaller than those in the left panel of Fig. 1 for the same primary IGW without critical levels.

However, the right panel of Fig. 3 demonstrates different behavior near the critical levels of the jet streams with maximum at 50 km altitude. There are two critical levels with $v_0 = c_h$ at altitudes of 33 and 67 km in the left panel of Fig. 3. In the vicinity of these critical levels in the right panel of Fig. 3 one can see destructions of inclined wave fronts of primary IGW and appearance of smaller-scale structures, which can indicate an increased production of secondary wave modes. This may be caused by a possible increase in the horizontal wind variance $\overline{u'^2}$ produced by the primary IGW, which is prescribed by the linear IGW theory near critical levels to maintain the vertical component of horizontal momentum $\rho_0 \overline{u'w'} \quad \rho_0 k \overline{u'^2}/(2m)$ at $|m| \to \infty$.

Studies of the spectrum of secondary waves in the AtmoSym model (Gavrilov and Kshevetskii, 2023, Efimov et al., 2023) showed prevailing amplitudes of spectral components with horizontal wavenumbers $k = 2\,k_0$ and $k = 3\,k_0$, where k_0 is the horizontal wavenumber of the primary IGW. The amplitudes of secondary wave modes are larger in the regions of increased amplitudes of the primary IGW. Due to large enough horizontal and vertical wavelengths, secondary waves might not substantially dissipate in the middle atmosphere and may form the layers with smaller-scale perturbations in the right panel of Fig. 3 near the critical levels.

The horizontal phase speeds of secondary waves modes may be different and they may propagate through the crit-

ical levels for the primary IGW. Therefore, layers with shorter-scale perturbations span above altitudes of the critical levels at 33 and 67 km in the right panel of Fig. 3. These secondary IGWs can transfer their energy through the critical levels. In the right panel of Fig. 3 at altitudes 33–67 km the wave fronts have inclinations to the horizon in opposite directions than those outside this layer. This is because the intrinsic frequency for IGWs with $c_x = 30$ m/s is negative between the lower and upper critical levels, $\omega < 0$, and to provide upward energy flux and positive vertical phase speed $c_z \sim -\omega/m$, the sign of vertical wavenumber m should be changed to the opposite. There might be also downward secondary IGWs.

Secondary waves generated near critical levels in the middle atmosphere may propagate to the higher atmospheric levels. In the right panel of Fig. 3 above 120 km altitude one can see 9–11 maxima and minima of vertical velocity, while the primary IGW form only four maxima and minima along the horizontal axis x at each height in the right panel of Fig. 1. This reveals substantial contribution from secondary wave modes with $k = 2\ k_0$ and $k = 3\ k_0$ in the upper atmosphere in the right panel of Fig. 3. Amplitudes of these secondary waves may reach 0.8 m/s in Fig. 3, which is much greater than respective amplitudes of 0.02 m/s for the primary IGW without critical levels in the right panel of Fig. 1.

Medvedev et al. (2023) supposed that despite larger amplitude of velocity perturbations, secondary waves may produce smaller vertical momentum flux because of their smaller horizontal and larger vertical wavelengths. Using the AtmoSym output we estimated averaged for horizontal plane located at altitude of 150 km IGW momentum flux for $c_x = 30$ m/s at the model time $t = 75$ h. For the windless atmosphere corresponding to the right panel of Fig. 1, the wave momentum flux at altitude 150 km is $F_m = \rho_0 \overline{u'w'} = 2.5{\cdot}10^{-14}$ N/m^2, and in the presence of critical levels in the middle atmosphere (Fig. 3) $F_m = 3.2{\cdot}10^{-10}$ N/m^2. Therefore, in our simulations higher-order wave modes over middle atmospheric critical levels have not only higher amplitudes, but also produce larger momentum fluxes in the thermosphere.

Vertical distances between consecutive inclined wave fronts in Figs. 1–3 are equal to local IGW vertical wavenumber, λ_z. At altitudes of 20 – 30 km, in the right panel of Fig. 1, $\lambda_z \approx 9.4$ km for the primary IGW having $c_h = 30$ m/s in the windless atmosphere. In the presence of jet stream in the right panel of Fig. 3 the inclined IGW fronts at altitudes of 20 – 30 km are noisier and λ_z vary between 8.5 – 10 km. Distances between consecutive wave fronts at altitudes 120–140 km in the right panel of Fig. 3 give values $\lambda_z \sim$ 13–18 km. This show that vertical wavelengths of secondary wave modes propagating to the upper atmosphere are substantially larger than λ_z of primary IGW at altitudes 20–30 km below the critical levels. Wave modes with longer λ_z are subjects to smaller dissipation due to molecular and turbulent viscosity and heat conductivity and they can propagate up to higher altitudes in the atmosphere (Vadas, 2007). This can explain higher amplitudes of secondary wave modes with larger λ_z at altitudes above 130 km in the right panel of Fig. 3 than the amplitude of shorter primary IGW in the right panel of Fig. 1, which is strongly dissipated in the thermosphere.

Zhao et al. (2017) and Becker and Vadas (2018) analyzed IGWs in the middle atmosphere using multiyear lidar observations of temperature variations in the middle atmosphere. They found that the IGW vertical wavelengths and horizontal phase speeds and λ_z at altitudes of 30–40 km are generally smaller than those simultaneously observed at higher altitudes in the mesosphere and lower thermosphere. Becker and Vadas (2018) used a GW-resolving high-resolution simulation and showed that secondary IGWs are generated just above the maximum wind speed of the polar vortex jet, and that these secondary waves have larger λ_z similar to the data from McMurdo (see Fig. 14 of that paper). The comparisons of the model data with the lidar data revealed that λ_z is smaller in the stratosphere and larger in the mesosphere, which is a result of the longer secondary IGWs in the mesosphere.

The study by Becker and Vadas (2018) was able to effectively reproduce the observations of Zhao et al (2017) via a GW-resolving model and showed that stratospheric waves can generate longer secondary waves, which can propagate to the upper atmosphere. Vadas et al. (2018) considered a mechanism of secondary IGW generating by body forces due to local accelerations of the mean flow and heat influxes produced by dissipation of primary waves. Such secondary IGWs propagating upwards may have vertical wavelengths longer than that of the primary waves (Vadas and Liu, 2013; Vadas and Becker, 2018). Decreasing λ_z near the critical level may cause increased dissipation of the primary IGW (see above) and, in addition, can activate generating secondary IGWs due to the body forces.

Vadas et al (2023a) showed the generation of IGWs by the polar vortex jet in the stratosphere and the generation of upward and downward propagating secondary wave modes at altitudes of 50–60 km over Europe, where the primary IGWs dissipated and produce body forces due to wave accelerations of the mean flow and heat influxes. The upward and downward propagating secondary IGWs were observed by Rayleigh lidar at ALOMAR in northern Norway and were simulated with the gravity wave resolving general circulation model HIAMCM (Vadas et al, 2023a).

Simulating IGWs from the ground to the thermosphere was made by Vadas et al. (2024). The authors showed that primary IGWs generated at the entrance, core and exit regions of the polar vortex jet dissipate and deposit momentum in the upper stratosphere/lower mesosphere, where the atmosphere responds by generating secondary wave modes. This course of action is reiterated, resulting in higher-order medium to large-scale IGWs in the thermosphere. These latter waves had much larger λ_z than the

primary IGWs. Simulated IGWs are in a good agreement with satellite, lidar and meteor radar observations (Vadas et al., 2024). Therefore, the middle atmosphere jet streams could lead to the global generation of higher-order medium to large-scale in the thermosphere by means of multi-step vertical interactions.

Simulations of the present paper confirm the importance of secondary waves in the perturbation of the upper atmosphere. Enhanced generation of secondary waves near critical levels in jet streams located in the middle atmosphere can increase AGW activity in the upper atmosphere. Our simulations show that the spectrum of secondary waves generated by the primary IGW in the middle atmosphere may contain components with longer vertical wavelengths, which are less dissipative and can produce substantial wave perturbations in the thermosphere. Critical levels of the background wind profile in the middle atmosphere may increase generation of secondary wave modes. Components of these secondary modes with longer vertical wavelengths propagating upwards may produce stronger IGW perturbations in the upper atmosphere than direct perturbations made by the primary IGW propagating in the same atmospheric conditions without the critical levels.

5. Conclusion

Using a high-resolution numerical model, the propagation of acoustic-gravity waves (AGWs) into the upper atmosphere is simulated. The background wind profile contains critical levels where the horizontal wind velocity is equal to the horizontal phase velocity of the primary AGW. According to the traditional theory of atmospheric waves, the vertical wavelength tends to zero near these levels. Consequently, AGW propagating from the troposphere should dissipate strongly and cannot reach higher layers of the atmosphere. This theory assumes the stationarity of the wave process, when the amplitudes and other parameters of the AGW do not change over time.

The numerical modeling involves wave sources in the form of plane wave perturbations of vertical velocity propagating along the Earth's surface. Upon activating the wave source, an initial AGW pulse occurs. Within a few minutes, it propagates to heights of 100 km and above, dissipating under the influence of strong viscosity and thermal conductivity. Subsequently, there is an interval to establish the wave process at all atmospheric altitudes, which can last up to several dozen periods of the wave source. During this transition period, the wave process is non-stationary.

Jet streams in the atmosphere are approximated with Gaussian profiles of the mean zonal wind. High-altitude jet stream with a maximum at 110 km and stratosphere-mesosphere flow with a maximum at 50 km are examined. Calculations reveal that in the scenario of high-altitude jet flow, the AGW reaches a critical level where the mean wind matches the phase speed of the primary wave. This causes a sharp decrease in vertical wavelength and leads to wave dissipation due to high molecular and turbulent viscosity. Consequently, above the high-altitude jet stream, the AGW's amplitude are significantly reduced compared to the case of absence of a jet stream.

In the case of a jet stream in the middle atmosphere, part of wave energy can pass through the critical layers and propagate further into the upper atmosphere. There is an increased generation of secondary wave modes in the critical level regions. Hence, the main secondary wave modes with horizontal length equal to half and one third of the wavelength of the primary AGW may dominate at altitudes exceeding 120 km. At high altitudes, the amplitudes of these secondary modes may surpass the amplitudes of the AGW in the absence of critical levels.

Declaration of competing interest

The authors declare that they have no known competing financial interests or personal relationships that could have appeared to influence the work reported in this paper.

Acknowledgments

Simulating nonstationary AGW fields was supported by Saint-Petersburg State University (research grant 116234986) and calculating and analysis of the wave spectra was supported by the Russian Science Foundation (Grant 20-77-10006-P).

References

Alexander, M.J., Geller, M., McLandress, C., Polavarapu, S., Preusse, P., Sassi, F., Sato, K., Eckermann, S., Ern, M., Hertzog, A., et al., 2010. Recent developments in gravity-wave effects in cli-mate models and the global distribution of gravity-wave momentum flux from observations and models. Q. J. R. Meteorol. Soc. Part A 136 (650), 1103–1124. https://doi.org/10.1002/qj.637.

AtmoSym, 2017. URL: http://atmos.kantiana.ru/language/ru (accessed June 10, 2024).

Bacmeister, J.T., Schoeberl, M.R., 1989. Breakdown of vertically propagating two-dimensional gravity waves forced by orography. J. Atmos. Sci. 46, 2109–2134.

Becker, E., Knopfel, R., Lubken, F.-J., 2015. Dynamically induced hemispheric differences in the seasonal cycle of the summer polar mesopause. J. Atmos. Solar-Terr. Phys. 129, 128–141. https://doi.org/10.1016/j.jastp.2015.04.014.

Becker, E., Goncharenko, L., Harvey, V.L., Vadas, S.L., 2022b. Multistep vertical coupling during the January 2017 sudden stratospheric warming. J. Geophys. Res. Space Phys. 127 (12). https://doi.org/10.1029/2022JA030866 e2022JA030866.

Becker, E., Vadas, S.L., 2018. Secondary gravity waves in the winter mesosphere: results from a high-resolution global circulation model. J. Geophys. Res. Atmos. 123 (5), 2605–2627. https://doi.org/10.1002/2017JD027460.

Becker, E., Vadas, S.L., 2020. Explicit global simulation of gravity waves in the thermosphere. J. Geophys. Res. Space Phys. 125 (10). https://doi.org/10.1029/2020JA028034.

Chen, C., Chu, X., Zhao, J., Roberts, B.R., Yu, Z., Fong, W., Lu, X., Smith, J.A., 2016. Lidar observations of persistent gravity waves with periods of 3–10 h in the Antarctic middle and up-per atmosphere at McMurdo (77.83° S, 166.67° E). J. Geophys. Res: Space Phys. 121, 1483–1502. https://doi.org/10.1002/2015JA022127.

Efimov, M. M., Gavrilov, N. M., Kshevetskii, S. P., Koval, A. V., 2023. Numerical simulation of the spectrum of secondary acoustic-gravity waves in the middle and upper atmosphere. In: Proceedings of SPIE 12780 (29th International Symposium on Atmospheric and Ocean Optics: Atmospheric Physics), 127807C. https://doi.org/10.1117/12.2690531.

Franco-Diaz, E., Gerding, M., Holt, L., Strelnikova, I., Wing, R., Baumgarten, G., Lübken, F.-J., 2024. Convective gravity wave events during summer near 54° N, present in both AIRS and Rayleigh–Mie–Raman (RMR) lidar observations. Atmos. Chem. Phys. 24, 1543–1558. https://doi.org/10.5194/acp-24-1543-2024.

Franke, P.M., Robinson, W.A., 1999. Nonlinear behavior in the propagation of atmospheric gravity waves. J. Atmos. Sci. 56, 3010–3027.

Fritts, D.C., Vadas, S.L., Wan, K., Werne, J.A., 2006. Mean and variable forcing of the middle atmosphere by gravity waves. J. Atmos. Solar-Terr. Phys. 68 (3–5), 247–265. https://doi.org/10.1016/j.jastp.2005.04.010.

Fritts, D.C., Wang, L., Werne, J., 2009. Gravity wave–fine structure interactions: a reservoir of small-scale and large-scale turbulence energy. Geophys. Res. Lett. 36 (19). https://doi.org/10.1029/2009GL039501 L19805.

Fritts, D.C., Wan, K., Werne, J., Lund, T., Hecht, J.H., 2014. Modeling the implications of Kelvin-Helmholtz instability dynamics for airglow observations. J. Geophys. Res.: Atmos. 119, 8858–8871. https://doi.org/10.1002/2014JD021737.

Gassmann, A., Herzog, H.-J., 2015. How is local material entropy production represented in a numerical model? Q. J. R. Meteorol. Soc. 2015 (41), 854–869. https://doi.org/10.1002/qj.2404.

Gavrilov, N.M., Kshevetskii, S.P., 2014. Numerical modeling of the propagation of nonlinear acoustic-gravity waves in the middle and upper atmosphere. Izvestiya. Atmos. Oceanic Phys. 50 (1), 66–72. https://doi.org/10.1134/S0001433813050046.

Gavrilov, N.M., Kshevetskii, S.P., Koval, A.V., 2015. Verifications of the high-resolution numerical model and polarization relations of atmospheric acoustic-gravity waves. Geosci. Model Dev. 8, 1831–1838. https://doi.org/10.5194/gmd-8-1831-2015.

Gavrilov, N.M., Kshevetskii, S.P., Koval, A.V., 2022. Decay times of atmospheric acoustic–gravity waves after deactivation of wave forcing. Atmos. Chem. Phys. 22, 13713–13724. https://doi.org/10.5194/acp-22-13713-2022.

Gavrilov, N.M., Kshevetskii, S.P., 2023. Identification of spectrum of secondary acoustic-gravity waves in the middle and upper atmosphere in a high-resolution numerical model. Solar-Terrestrial Phys. 9 (3), 86–92. https://doi.org/10.12737/stp-93202310.

Geller, M.A., Alexander, M.J., Love, P.T., Bacmeister, J., Ern, M., Hertzog, A., Manzini, E., Preusse, P., Sato, K., Scaife, A.A., Zhou, T., 2013. A comparison between gravity wave momentum fluxes in observations and climate models. J. Climate 26 (17), 6383–6405. https://doi.org/10.1175/JCLI-D-12-00545.1.

Gossard, E.E., Hooke, W.H., 1975. Waves in the atmosphere: atmospheric infrasound and gravity waves: their generation and propagation. Elsevier Sci. Publ. Co., (Dev. Atmos. Sci. 2), 470.

Heale, C.J., Inchin, P.A., Snively, J.B., 2022. Primary versus secondary gravity wave responses at F-region heights generated by a convective source. J. Geophys. Res.: Space Phys. 127. https://doi.org/10.1029/2021JA029947 e2021JA029947.

Holton, J.R., 1983. The influence of gravity wave breaking on the general circulation of the middle atmosphere. J. Atmos. Sci. 40, 2497–2507.

Kikoin, I.K., 1976. In: Tables of Physical Quantities. Atomizdat Publ., Moscow, pp. 272–279.

Larsen, M.F., 2000. A shear instability seeding mechanism for quasiperiodic radar echoes. J. Geophys. Res. 105, 24931–24940.

Larsen, M.F., Yamamoto, M., Fukao, S., Tsunoda, R.T., Saito, A., 2005. Observations of neutral winds, wind shears, and wave structure during a sporadic- E/QP event. Ann. Geophys. 23, 2369–2375. https://doi.org/10.5194/angeo-23-2369-2005.

Li, Q., Xu, J., Liu, H., Liu, X., Yuan, W., 2022. How do gravity waves triggered by a typhoon propagate from the troposphere to the upper atmosphere? Atmos. Chem. Phys. 22, 12077–12091. https://doi.org/10.5194/acp-22-12077-2022.

Liu, X., Xu, J., Liu, H., Ma, R., 2008. Nonlinear interactions be-tween gravity waves with different wavelengths and diurnal tide. J. Geophys. Res.: Atmos. 1139 (8). https://doi.org/10.1029/2007JD009136 D08112.

Lund, T.S., Fritts, D.C., 2012. Numerical simulation of gravity wave breaking in the lower thermosphere. J. Geophys. Res. 117. https://doi.org/10.1029/2012JD017536 D21105.

Medvedev, A.S., Gavrilov, N.M., 1995. The nonlinear mechanism of gravity wave generation by meteorological motions in the atmosphere. J. Atmos. Terr. Phys. 57, 1221–1231.

Medvedev, A.S., Klaassen, G.P., Yiğit, E., 2023. On the dynamical importance of gravity wave sources distributed over different heights in the atmosphere. J. Geophys. Res.: Space Phys. 128. https://doi.org/10.1029/2022JA031152 e2022JA031152.

Miyoshi, Y., Fujiwara, H., 2008. Gravity waves in the thermo-sphere simulated by a general circulation model. J. Geophys. Res.: Atmos. 113 (1). https://doi.org/10.1029/2007JD008874 D01101.

Miyoshi, Y., Fujiwara, H., Jin, H., Shinagawa, H., 2014. Global view of gravity waves in the thermosphere simulated by a general circulation model. J. Geophys. Res.: Space Phys. 119 (7), 5807–5820. https://doi.org/10.1002/2014JA019848.

Picone, J.M., Hedin, A.E., Drob, D.P., Aikin, A.C., 2002. NRLMSISE-00 empirical model of the atmosphere: statistical comparisons and scientific issues. J. Geophys. Res. 107 (A12), 1468. https://doi.org/10.1029/2002JA009430.

Smith, R.B., Nugent, A.D., Kruse, C.G., Fritts, D., Doyle, J.D., Eckermann, S.D., Taylor, M.J., Dörnbrack, A., Uddstrom, M., Cooper, W., Romashkin, P., Jensen, J., Beaton, S., 2016. Stratospheric gravity wave fluxes and scales during DEEPWAVE. J. Atmos. Sci. 73 (7), 2581–2869. https://doi.org/10.1175/JAS-D-15-0324.1.

Townsend, A.A., 1965. Excitation of internal waves by a turbulent boundary layer. J. Fluid Mech. 22, 241–252.

Townsend, A.A., 1966. Internal waves produced by a convective layer. J. Fluid Mech. 24, 307–319.

Vadas, S.L., 2007. Horizontal and vertical propagation and dissipation of gravity waves in the thermosphere from lower atmospheric and thermospheric sources. J. Geophys. Res. 112. https://doi.org/10.1029/2006JA011845 A06305.

Vadas, S.L., Azeem, I., 2021. Concentric secondary gravity waves in the thermosphere and ionosphere over the continental United States on 25-26 March 2015 from deep convection. J. Geophys. Res. Space Phys. 126 (2). https://doi.org/10.1029/2020JA028275 e2020JA028275.

Vadas, S.L., Becker, E., 2019. Numerical modeling of the generation of tertiary gravity waves in the mesosphere and thermosphere during strong mountain wave events over the Southern Andes. J. Geophys. Res. Space Phys. 124, 7687–7718. https://doi.org/10.1029/2019JA026694.

Vadas, S.L., Crowley, G., 2017. Neutral wind and density perturbations in the thermosphere created by gravity waves observed by the TIDDBIT sounder. J. Geophys. Res.: Space Phys. 122, 6652–6678. https://doi.org/10.1002/2016JA023828.

Vadas, S.L., Becker, E., Figueiredo, C.A.O.B., Bossert, K., Harding, B., Gasque, C., 2023b. Primary and secondary gravity waves and global wind changes generated by the Tonga volcanic eruption on 15 January 2022: modeling and comparison with ICON-MIGHTI winds. J. Geophys. Res. Space Phys. 128. https://doi.org/10.1029/2022JA031138 e2022JA031138.

Vadas, S.L., Figueiredo, C.A.O.B., Becker, E., Huba, J.D., Themens, D. R., Hindley, N.P., Galkin, I., Bossert, K., 2023c. Traveling ionospheric disturbances induced by the secondary gravity waves from the Tonga eruption on 15 January 2022: Modeling with MESORAC-HIAMCM-SAMI3 and comparison with GPS/TEC and ionosonde data. J. Geophys. Res. Space Phys. 128. https://doi.org/10.1029/2023JA031408 e2023JA031408.

Vadas, S.L., Becker, E., Bossert, K., Hozumi, Y., Stober, G., Harvey, V. L., Baumgarten, G., Hoffmann, L., 2024. The role of the polar vortex jet for secondary and higher-order gravity waves in the northern

mesosphere and thermosphere during 11–14 January 2016. J. Geophys. Res.: Space Phys. 129 (9). https://doi.org/10.1029/2024JA032521 e2024JA032521.

Vadas, S.L., Fritts, D.C., Alexander, M.J., 2003. Mechanism for the generation of secondary waves in wave breaking regions. J. Atmos. Sci. 60 (1), 194–214. https://doi.org/10.1029/2004JD005574.

Vadas, S.L., Liu, H.-L., 2013. Numerical modeling of the large-scale neutral and plasma responses to the body forces created by the dissipation of gravity waves from 6 h of deep convection in Brazil. J. Geophys. Res.: Space Phys. 118, 2593–2617. https://doi.org/10.1002/jgra.50249.

Vadas, S.L., Zhao, J., Chu, X., Becker, E., 2018. The excitation of secondary gravity waves from local body forces: theory and observation. J. Geophys. Res. Atmos. 123 (17), 9296–9325. https://doi.org/10.1029/2017JD027970.

Vadas, S.L., Becker, E., Bossert, K., Baumgarten, G., Hoffmann, L., Lynn Harvey, V., 2023a. Secondary gravity waves from the stratospheric polar vortex over ALOMAR Observatory on 12-14 January 2016. J. Geophys. Res.: Atmos. 128. https://doi.org/10.1029/2022JD036985 e2022JD036985.

Yu, Y., Hickey, M.P., Liu, Y., 2009. A numerical model characterising internal gravity wave propagation into the upper atmosphere. Adv. Space Res. 44, 836–846. https://doi.org/10.1016/j.asr.2009.05.014.

Zhao, J., Chu, X., Chen, C., Lu, X., Fong, W., Yu, Z., Jones, R.M., Roberts, B.R., Dörnbrack, A., 2017. Lidar observations of stratospheric gravity waves from 2011 to 2015 at McMurdo (77.84° S, 166.69° E), Antarctica: 1. Vertical wavelengths, periods, and frequency and vertical wave number spectra. J. Geophys. Res.: Atmos. 122 (10), 5041–5062. https://doi.org/10.1002/2016JD026368.